

Efficient *ab initio* many-body calculations based on sparse modeling of Matsubara Green's function

Hiroshi Shinaoka^{1*}, Naoya Chikano¹, Emanuel Gull², Jia Li², Takuya Nomoto³, Junya Otsuki⁴, Markus Wallerberger⁵, Tianchun Wang³, Kazuyoshi Yoshimi⁶

1 Department of Physics, Saitama University, Saitama 338-8570, Japan

2 University of Michigan, Ann Arbor, Michigan 48109, USA

3 Department of Applied Physics, University of Tokyo, Japan

4 Research Institute for Interdisciplinary Science, Okayama University, Okayama 700-8530, Japan

5 Institute of Solid State Physics, TU Wien, 1040 Vienna, Austria

6 Institute for Solid State Physics, University of Tokyo, Chiba 277-8581, Japan

* h.shinaoka@gmail.com

June 25, 2021

Abstract

This lecture note reviews recently proposed sparse-modeling approaches for efficient *ab initio* many-body calculations based on the data compression of Green's functions. The sparse-modeling techniques are based on a compact orthogonal basis representation, intermediate representation (IR) basis functions, for imaginary-time and Matsubara Green's functions. A sparse sampling method based on the IR basis enables solving diagrammatic equations efficiently. We describe the basic properties of the IR basis, the sparse sampling method and its applications to *ab initio* calculations based on the *GW* approximation and the Migdal-Eliashberg theory. We also describe a numerical library for the IR basis and the sparse sampling method, `irbasis`, and provide its sample codes. This lecture note follows the Japanese review article [H. Shinaoka *et al.*, Solid State Physics **56**(6), 301 (2021)].

Contents

1	Introduction	2
2	Intermediate-representation (IR) of Matsubara Green's functions	3
3	Sparse sampling	6
3.1	Dyson equation	6
3.2	Sparse sampling and Fourier transform	7
3.3	Notes on calculations using the sparse sampling method	10
4	Review of applications	11
4.1	Noble-gas atoms, silicon crystals: Self-consistent <i>GW</i> and second-order perturbation (GF2) calculations	11

4.2	First-principles calculations of superconducting transition temperature based on Migdal-Eliashberg equation	13
4.3	Calculation of magnetic interaction based on Lichtenstein formula	14
4.4	Other applications	15
5	irbasis library	15
5.1	Installation	15
5.2	Dimensionless form	16
5.3	Evaluation of IR basis functions	16
5.4	Example: Second-order perturbation theory	17
6	Summary and future perspectives	19
A	Some properties of the IR basis functions	21
B	Numerical stability of sparse sampling	22
References		24

1 Introduction

Perturbation and quantum field theories based on Green's functions are widely used for *ab initio* and quantum many-body calculations. The imaginary-time formalism based on Matsubara Green's functions is well known for its simplicity in numerical treatment. It has been used for *ab initio* calculations and model calculations based on various theories such as *GW* [1], the random phase approximation (RPA) [2], fluctuation exchange (FLEX) [3, 4], dynamical mean-field theory (DMFT) [5], and quantum Monte Carlo methods [6]. Most readers who are interested in this study may have experienced such computational methods. The application of imaginary-time formalism is not limited to condensed matter physics but is also used in quantum chemistry and high energy physics [7–9].

Although it is used in a wide range of fields, its efficient numerical handling has yet to be fully established. For example, in *ab initio* calculations, it is necessary to simultaneously deal with multiple energy scales that differ by orders of magnitude. A typical example is the width of low-energy bands (several to several tens of eV) and the low temperature at which physical phenomena occur ($1 \text{ K} \simeq 0.1 \text{ meV}$). In such a case, the number of imaginary (Matsubara) frequencies required in the calculations increases, and the computation time and the amount of memory required increase to an unmanageable level.

Furthermore, calculations at the two-particle level (e.g., susceptibility calculations using the Bethe-Salpeter equation) require the handling of vertex functions and depend on multiple imaginary frequencies. Therefore, calculations with full frequency dependence are extremely costly even for simple model calculations, which hinders their application in realistic materials. In this article, we review efficient many-body and *ab initio* calculation methods based on the data compression of Matsubara Green's functions. A compact basis for Matsubara Green's function, the intermediate representation (IR), was discovered in 2017 [10, 11]. In 2020, an

efficient calculation method based on sparse sampling was developed [12]. Since then, its applications in *ab initio* calculations have been rapidly spreading [13–17].

This article summarizes the results of the rapid theoretical progress made during the last few years and provides a comprehensive overview of the 1) basic properties of the IR basis, 2) sparse sampling method for fast computation of diagrammatic equations, and 3) numerical library `irbasis` [18]. This is intended to help readers enter the field.

2 Intermediate-representation (IR) of Matsubara Green's functions

The intermediate representation (IR) is a basis set that can expand the imaginary frequency and time dependence of the two-point imaginary-time/-frequency correlation function [10]. Let us summarize its definition and properties.

The general definition of the imaginary-time two-point correlation function is given by

$$\hat{G}^\alpha(i\omega) = \int_0^\beta d\tau e^{i\omega\tau} \langle T_\tau A^\alpha(\tau) B^\alpha(0) \rangle, \quad (1)$$

where $\beta = 1/T$ is the inverse temperature, τ is the imaginary time, T_τ is the time ordering operator, and α is either F (fermion) or B (boson). Here, we take $k_B = 1$. In addition, A and B are the operators, and $i\omega$ is an imaginary frequency corresponding to the statistics α . We attach a hat $\hat{\cdot}$ to the quantities defined in an imaginary frequency space. In the important special case of a one-particle Green's function, A is an annihilation operator, and B is a creation operator.

The Lehmann representation of the two-point correlation function is given as follows:

$$\hat{G}(i\omega) = \int_{-\omega_{\max}}^{\omega_{\max}} d\omega' \underbrace{\frac{(\omega')^{\delta_{\alpha,B}}}{i\omega - \omega'}}_{K^\alpha(i\omega, \omega')} \rho(\omega'), \quad (2)$$

where $\rho(\omega)$ is a corresponding spectral function. Here, we take ω_{\max} to be sufficiently large such that the spectral function $\rho(\omega)$ is nonzero only for $\omega \in [-\omega_{\max}, \omega_{\max}]$. The notation $\omega'^{\delta_{\alpha,B}}$ evaluates to 1 for $\alpha=F$ and ω' for $\alpha=B$, respectively. This expresses the fact that we add a factor ω' in the bosonic case in order to regularize the denominator, a trick commonly employed in numerical analytic continuation.¹ The spectral function can be inferred from the Kramers–Kronig relations from the (retarded) real-frequency Green's function:

$$\rho(\omega) = -\frac{\omega^{\delta_{\alpha,B}}}{\pi} \text{Im} \hat{G}(\omega + i0^+). \quad (3)$$

The integral equation (2) connects the spectral and response functions through the kernel $K^\alpha(i\omega, \omega)$. Since temperature is finite, the spectral function $\rho(\omega)$ is given by a finite set of delta peaks plus a smooth function of ω .

¹We note that this regularization comes at a price: the bosonic kernel $K^B(i\omega, \omega)$ in Eq. (2) annihilates any structure of the spectral function at $\omega = 0$. Therefore, the bosonic IR basis, which is defined below, cannot represent such zero-energy structures. A workaround, which augments the IR basis, is discussed in Ref. [19].

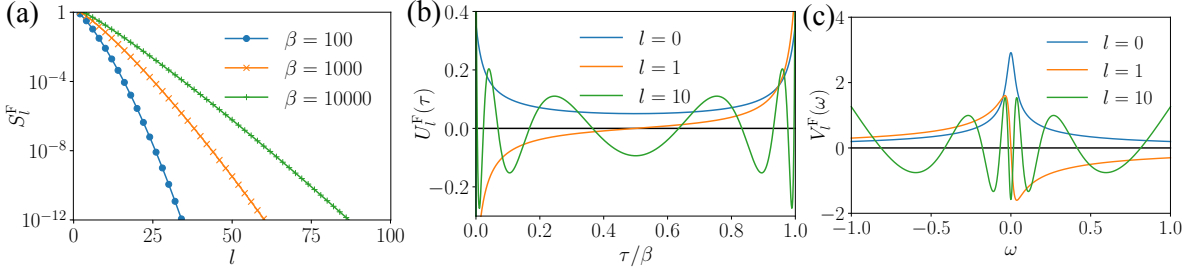


Figure 1: (a) Singular value S_l^α computed for various values of β , (b), (c) IR basis functions $U_l^\alpha(\tau)$ and $V_l^\alpha(\omega)$ computed for $\beta = 100$. Here, we present the results for fermions and $\omega_{\max} = 1$. The data were calculated using `irbasis` [18].

The task at hand is to find a representation of the imaginary-frequency $\hat{G}(i\omega)$ which retains the maximum amount of information about the physical, real-frequency $\rho(\omega)$. For this, we perform a singular value expansion of the kernel K connecting the two objects for a given β and ω_{\max} [10]:

$$K^\alpha(i\omega, \omega') = \sum_{l=0}^{\infty} \hat{U}_l^\alpha(i\omega) S_l^\alpha V_l^\alpha(\omega'). \quad (4)$$

In the imaginary-time domain, the singular value expansion can be expressed as

$$K^\alpha(\tau, \omega') \equiv \frac{1}{\beta} \sum_{i\omega} K^\alpha(i\omega, \omega') e^{-i\omega\tau} = \sum_{l=0}^{\infty} U_l^\alpha(\tau) S_l^\alpha V_l^\alpha(\omega'). \quad (5)$$

The singular value expansion has similar properties as the singular value decomposition of matrices: the singular values S_l satisfy $S_0 > S_1 > \dots > 0$. The left singular functions $\{U_0(\tau), U_1(\tau), \dots\}$ form an orthonormal set on the imaginary time axis $\tau \in [0, \beta]$, while the right singular functions $\{V_0(\tau), V_1(\tau), \dots\}$ form an orthonormal set on the real frequency axis $\omega \in [-\omega_{\max}, \omega_{\max}]$.

The so-called IR basis is nothing but the left singular vector $\hat{U}_l^\alpha(i\omega)$ [$U_l^\alpha(\tau)$] and the right singular vector $V_l^\alpha(\omega)$. It should be emphasized that the IR basis is determined only by the inverse temperature β , statistical properties α , and the energy (frequency) cutoff ω_{\max} and does not depend on the details of the system.

Figure 1 shows the singular values S_l^α and the IR basis functions $U_l^\alpha(\tau)$ and $V_l^\alpha(\omega)$ for fermions. The IR basis functions have the following interesting properties, which can be verified numerically:²

Property 1 The singular values S_l^α are non-degenerate, non-negative, and monotonically decrease faster than exponentially with respect to l .

Property 2 The number of numerically significant singular values (e.g., $S_l^\alpha/S_0^\alpha \geq 10^{-15}$) is determined by the dimensionless quantity $\Lambda \equiv \beta\omega_{\max}$ and increases only logarithmically with respect to Λ .

²Note that the analytical form of the IR basis has yet to be determined. If you are good at mathematics, please give it a try.

Property 3 $U_l^\alpha(\tau)$ and $V_l^\alpha(\omega)$ can be chosen to be real functions, and they then become even-odd functions for even-odd l . In this convention, $\hat{U}_l^\alpha(i\omega)$ is purely imaginary or real.

Property 4 $U_l^\alpha(\tau)$ and $V_l^\alpha(\omega)$ have l roots. In addition, in the limit of $\beta\omega_{\max} \rightarrow 0$ (a high-temperature limit), $U_l^\alpha(\tau(x))$ and $V_l^\alpha(\omega(x))$ coincide with the Legendre polynomial $P_l(x)$ up to a constant [$\tau(x) \equiv \beta(x+1)/2$, $\omega(x) \equiv x\omega_{\max}$ for $-1 < x < 1$]³.

We sketch mathematical proofs of these properties in Appendix A.

Now, let us expand an “arbitrary” two-point correlation using L IR basis functions:

$$\hat{G}^\alpha(i\omega) = \sum_{l=0}^{L-1} \hat{U}_l^\alpha(i\omega) G_l^\alpha + \epsilon_L. \quad (6)$$

If the corresponding spectral function is finite only in the interval $[-\omega_{\max}, \omega_{\max}]$, the expansion factor G_l^α can be obtained using the fact that the IR functions form an orthonormal set.

$$G_l^\alpha = S_l^\alpha \int_{-\omega_{\max}}^{\omega_{\max}} d\omega \rho^\alpha(\omega) V_l^\alpha(\omega) \equiv S_l^\alpha \rho_l \quad (7)$$

From Eq. (7), it can be seen that G_l^α vanishes at least as fast as S_l^α , i.e., faster than the exponential function from “Property 1.”

Let us now introduce a practical example that demonstrates the compactness of the IR. Figure 2 shows the convergence of the expansion coefficients ρ_l and G_l for some simple spectral functions. The convergence properties of ρ_l strongly depend on the shape of the spectral function. In general, ρ_l decays exponentially in the case of a smooth spectral function, but not in the case of a δ function. By contrast, G_l always decays as fast as or even faster than the singular values, regardless of the details of the spectral functions. We would like to emphasize again that this convergence is determined by the singular value of the kernel and does not depend on the details of the system.

In Eq. (7), we can see that when we transform G_l into ρ_l , ρ_l is suppressed by the singular values exponentially at a large l . This means that some of the information in the spectral function is lost in the transformation to the imaginary-time domain. Thus, it is usually difficult to recover the exact spectral function from the numerical data of the Matsubara Green’s function. This is because, in the inverse transformation $\rho_l = (S_l^\alpha)^{-1} G_l$, the error of G_l is amplified at small singular values. Many approximate methods based on different principles have been proposed to prevent this problem, such as the maximum entropy and SpM methods [11, 21]; however, we will not discuss this topic here.

The main focus of this article is to take advantage of the fact that the Matsubara Green’s function has less information than its real-frequency counterpart, and to speed up the computation within the imaginary-time-frequency domain. In this respect, the IR basis $\hat{U}_l^\alpha(i\omega)$ and $U_l^\alpha(\tau)$ efficiently represent the remaining information in imaginary-time quantities.

Finally, we present a numerical example that demonstrates the advantages of the IR basis at low temperatures. Figure 3 shows the β -dependence of the number of basis functions required to represent the Green’s function within a given accuracy. Specifically, assuming the

³As a compact basis for imaginary-time Green’s functions, the Legendre polynomial basis [20] is conventionally used in the context of DMFT and QMC. This fact is interesting because it shows that the Legendre polynomial basis corresponds to the high-temperature limit of the IR basis.

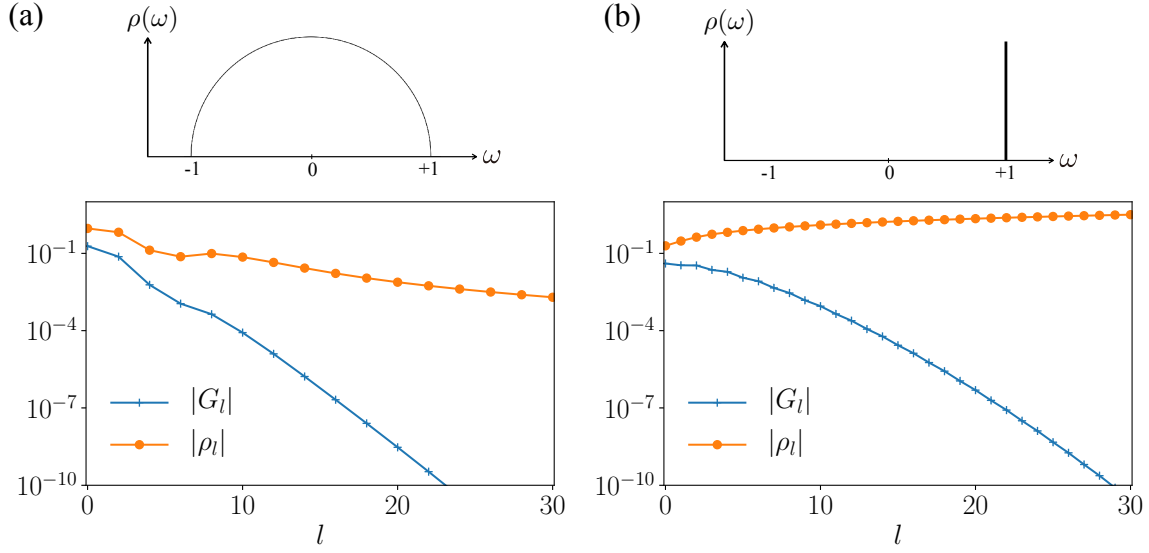


Figure 2: IR expansion coefficients G_l (Green's function) and ρ_l (spectral function) for (a) a semicircular spectral function and (b) an insulating spectral function. We take $\beta = 100$, $\omega_{\max} = 1$, and $\alpha = F$. The data were calculated using `irbasis` [18]. In (a), G_l and ρ_l for an odd l are not plotted because they are values of zero.

same spectral function as in Figure 2 (b), we calculate the number of bases required to represent $G(\tau = 0)$ with an accuracy of 10^{-8} ⁴. As expected from Fig. 1(a), the required number of IR basis functions increases logarithmically. By contrast, in the case of the imaginary frequency (Matsubara) representation and the Legendre basis [20], the number of required basis functions increases proportionally to $O(\beta)$ and $O(\sqrt{\beta})$, respectively. The difference from the IR basis becomes significant at lower temperatures.

3 Sparse sampling

3.1 Dyson equation

In the previous section, we showed that Matsubara Green's function can be represented compactly using the IR basis. A natural question is whether or not we can efficiently solve diagrammatic equations in the imaginary-time formalism. As an example, let us consider the Dyson equation

$$\hat{G}(i\omega) = \frac{1}{i\omega + \mu - \mathcal{H} - \hat{\Sigma}(i\omega)}, \quad (8)$$

⁴In the result of the imaginary frequency (Matsubara) representation, we count the number of nonnegative imaginary frequencies. A second-order high-frequency expansion is applied in the Fourier transform into $G(\tau)$.

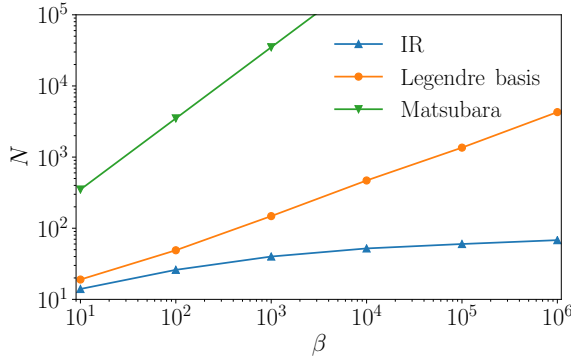


Figure 3: β dependence of the number of basis functions needed to represent Green's function with high accuracy. We used the same spectral function as in Figure 2(b). We counted the minimum number of basis functions required to represent $G(\tau = 0)$ with an accuracy of 10^{-8} . For $\omega_{\max}\beta > 10^4$, the advantage of the IR basis ($\omega_{\max} = 1$) is remarkable.

where we take $\mathcal{H} = 0$ and $\mu = 0$ for the sake of simplicity of demonstration. The self-energy $\hat{\Sigma}(i\omega)$ can also be compactly expanded on an IR basis:

$$\hat{\Sigma}(i\omega) \simeq \sum_{l=0}^{L-1} \Sigma_l \hat{U}_l^F(i\omega). \quad (9)$$

Here, we excluded the Hartree term for simplicity. The question is whether the expansion coefficients of Eq. (16), G_l , can be computed efficiently from the given Σ_l .

Solving the Dyson equation directly in the IR basis is not the best way. To see this, we transform the Dyson equation into a linear equation for $\hat{G}(i\omega)$ as

$$\sum_{i\omega'} A_{i\omega, i\omega'} \hat{G}(i\omega') = 1. \quad (10)$$

Note that the linear operator is defined as $A_{i\omega, i\omega'} \equiv \delta_{i\omega, i\omega'}(i\omega - \hat{\Sigma}(i\omega))$, where only the diagonal component remains for the imaginary frequency. In principle, we can transform $A_{i\omega, i\omega'}$ and $\hat{G}(i\omega')$ into an IR basis. However, in the transformed linear equation, the linear operator is no longer diagonal, and we need to solve the linear equation of size $L \times L$. Therefore, the computational cost of the Dyson equation scales as $O(N_{\text{band}}^3 L^3) = O(N_{\text{band}}^3 (\log(\beta\omega_{\max}))^3)$ for multiband systems. This computational complexity grows more slowly than any power of $\beta\omega_{\max}$. Although this is thus asymptotically faster than the conventional approach, this method is not advantageous for typical parameters, $N_{\text{band}} = 100$ and $L \simeq 100$.

How can we simultaneously benefit from the compactness of the representation on an IR basis and the diagonality of the Dyson equation? We will answer this question in the next section.

3.2 Sparse sampling and Fourier transform

The sparsity of information can be exploited to reduce the computational complexity of the diagrammatic equations either by the sparse sampling method [12] or the minimax isometry

	Memory cost	Truncation error	Runtime cost
Sparse sampling	$L = O(\log(\omega_{\max}\beta))$	$O(e^{-\alpha L})$	$O(L^2)$
Conventional method (FFT)	$N_\omega = O(\omega_{\max}\beta)$	$O(1/N_\omega^\gamma)$	$O(N_\omega \log N_\omega)$

Table 1: Comparison between the sparse sampling method and the conventional method. The power γ (≥ 1) depends on the details of the high-frequency expansion.

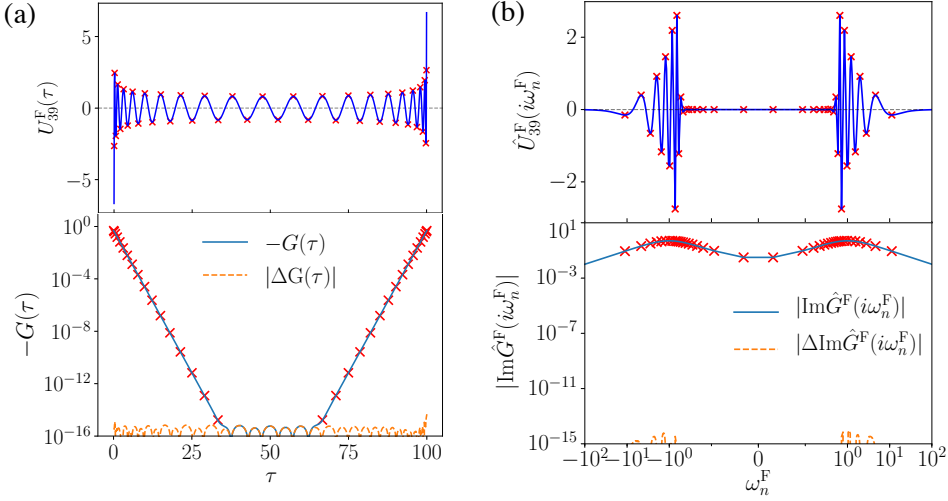


Figure 4: Basis functions ($l = 39$) were used to generate sampling points for (a) imaginary times and (b) imaginary frequencies. We also show the Green's function reconstructed by sparse sampling (solid line) as well as its deviation from the exact value (dashed line). The exact Green's function is not shown because it is nearly identical to the reconstructed value. We used the semicircular model shown in Fig. 2(a) ($\beta = 100$, $\omega_{\max} = 1$). Revised version of Fig. 2 in Ref. [12].

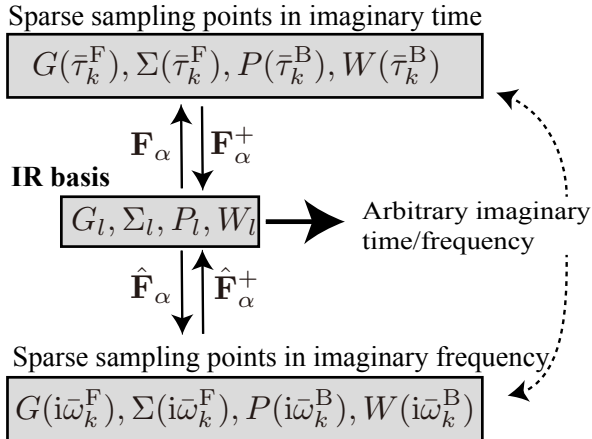


Figure 5: Overview of the sparse sampling method. One can efficiently transform data between sparse grids in the imaginary frequency and time domains through the IR basis. The data can be evaluated at any frequency and time once the IR expansion coefficients are known.

method [22]. Before introducing the sparse sampling method, we discuss how to extract information efficiently from the information on the imaginary frequency axis.

The inverse transformation of the expression in Eq. (6) is

$$G_l = \sum_{i\omega=-i\infty}^{i\infty} \hat{U}_l^F(i\omega)^* \hat{G}(i\omega). \quad (11)$$

To determine G_l from this equation, we need information regarding $\hat{G}(i\omega)$ within the total imaginary frequency domain. However, we do not need to evaluate this equation in practice because the frequency dependence of $\hat{G}(i\omega)$ has only L degrees of freedom at most, as shown in Fig. 2. Therefore, if we choose the appropriate L imaginary frequencies $i\omega$ and know the values of $\hat{G}(i\omega)$ at those points, we should be able to determine the values of G_l for all $l = 0, \dots, L-1$. We call these “appropriate frequencies” “sampling frequencies.”

The selection of sampling frequencies is not unique. In particular, we use the fact that $\hat{U}_l^\alpha(i\omega)$ has a sign structure similar to a polynomial (“Property 5”), and choose the maximum and minimum neighborhoods of $\hat{U}_{L-1}^\alpha(i\omega)$ (see Fig. 4).

$$\mathcal{W}^\alpha = \{i\omega_1^\alpha, i\omega_2^\alpha, \dots, i\omega_L^\alpha\}. \quad (12)$$

Given the values of the Green’s function on the sampling frequencies, we can easily calculate G_l^α as

$$\begin{aligned} G_l &= \underset{G_l}{\operatorname{argmin}} \sum_{i\omega \in \mathcal{W}^\alpha} \left| \hat{G}(i\omega) - \sum_{l=0}^{L-1} \hat{U}_l^\alpha(i\omega) G_l \right|^2 \\ &= \left(\hat{\mathbf{F}}_\alpha^+ \hat{\mathbf{g}} \right)_l \end{aligned} \quad (13)$$

using the least-squares fitting. Here, $\hat{\mathbf{F}}_\alpha^+$ is the Moore-Penrose pseudo-inverse of $\hat{\mathbf{F}}_\alpha$, which is defined as follows: $\hat{\mathbf{F}}_\alpha$ is a matrix consisting of the values of the basis functions at the sampling frequencies defined as $(\hat{\mathbf{F}}_\alpha)_{kl} = \hat{U}_l^\alpha(i\omega_k^\alpha)$. By contrast, $\hat{\mathbf{g}}$ is a vector consisting of the values of the fitted Green’s function, defined as $(\hat{\mathbf{g}})_k = \hat{G}^\alpha(i\omega_k^\alpha)$. Because $\hat{\mathbf{F}}$ is a small matrix of at most 100×100 , as long as the sampling frequencies are chosen as described above, the fitting procedure is numerically stable (refer to Sec. 3.3 and Appendix B). Once $\hat{\mathbf{F}}^+$ is computed, Eq. (13) is a matrix-vector product: The computational complexity is $O(L^2)$, and fast libraries such as BLAS can be used.

Similar sampling points in imaginary time can also be constructed by considering the sign structure of the IR basis $U_l^\alpha(\tau)$ in imaginary time. Let us write the result to the following:

$$\begin{aligned} G_l^\alpha &= \underset{G_l}{\operatorname{argmin}} \sum_k \left| \hat{G}^\alpha(\bar{\tau}_k^\alpha) - \sum_{l=0}^{L-1} \hat{U}_l^\alpha(\bar{\tau}_k^\alpha) G_l^\alpha \right|^2 \\ &= (\mathbf{F}_\alpha^+ \mathbf{g})_l. \end{aligned} \quad (14)$$

Here, $\bar{\tau}_k^\alpha$ are the sampling points, and we define $(\mathbf{F}_\alpha)_{kl} = U_l^\alpha(\bar{\tau}_k^\alpha)$.

Now, let us numerically demonstrate that the sparse sampling method can actually calculate the expansion coefficient G_l with high accuracy. Figures 4(a) and (b) show the sampling points at $\omega_{\max} = 1$ and $\beta = 100$, respectively. We also show the IR basis functions used

to generate the sampling points. It can be clearly seen that the basis functions have sign changes. The imaginary-time sampling points are densely distributed within the vicinity of $\tau = 0$ and β , where the Green's function rapidly changes its value [see Fig. 4(a)]. By contrast, at imaginary frequencies, the distribution of sampling points is dense at low frequencies and sparse at high frequencies, where the Green's function essentially has no structure [see Fig. 4(b)]. Figures 4(a) and (b) show expansion coefficients G_l reconstructed from the data on the sampling points as well as the reconstructed Green's functions from G_l . The reconstructed Green's functions agree with the exact values with an accuracy of approximately 15 digits, indicating the accuracy and numerical stability of the sparse sampling method.

Some may wonder why we can determine the expansion coefficient G_l of $l < L-1$ accurately using the sampling points determined from the structure of $U_{L-1}^\alpha(\tau)$ and $U_{L-1}^\alpha(i\omega)$. In fact, the distribution of the roots (zeros) of the IR basis functions for $l < L-1$ is always sparser than that of the basis functions for $l = L-1$ (Figure 1)⁵. Therefore, the sampling points determined from the basis functions of $l = L-1$ capture the sign change of the basis functions of $l < L-1$. For this reason, they serve as good sampling points for lower-order basis functions.

We now have all ingredients of the sparse sampling method. Henceforth, the sampling points at imaginary frequency and imaginary time will be referred to as the “sparse grid”⁶. As shown in Fig. 5, we can efficiently transform the data between the sparse grid and IR basis at imaginary frequencies and imaginary times. Once the expansion coefficients in the IR basis are obtained, the Green's function can be evaluated at any frequency or time. In this sense, sparse sampling is a physically motivated interpolation method for imaginary-time and imaginary-frequency quantities.

The sparse sampling method allows us to solve the Dyson Eq. (16) only on the sampling frequencies (grid). The exact imaginary frequency/time dependence can be reproduced from these values on the sparse grid.

Traditionally, when one wants to transform data between imaginary frequency and time, the fast Fourier transform is the standard method. Table 1 shows a comparison between the conventional method and the sparse sampling method. As the main feature of the sparse sampling method and based on the data size, the computational complexity increases more slowly than any power of β and bandwidth ω_{\max} .

Note that the sparse sampling method can also be used in combination with conventional polynomial bases [12].

3.3 Notes on calculations using the sparse sampling method

In practical applications of the sparse sampling method, one should take care not to introduce large systematic errors in the basis representation as defined in Eq. (6), such as large truncation errors ϵ_L due to insufficient basis size L or control parameter Λ . Such a systematic error may be amplified in the “fitting” procedure of Eqs. (13) and (14), leading to a large numerical error. Therefore, to ensure stable numerical calculations with the sparse sampling method, one should choose the appropriate basis parameters L and Λ such that the basis representation stays accurate. Please refer to Appendix B for more discussion on the numerical stability of the sparse sampling method.

⁵More precisely, for $l' < l$, between two adjacent roots of $U_{l'}^\alpha(\tau)$, $U_l^\alpha(\tau)$ contains one or more roots. In the case of $l = l' + 1$, this is mathematically proven. In a general case, no counterexample was found in the numerical experiments.

⁶The minimax isometry method [22] uses a similar sparse grid.

4 Review of applications

In the previous section, we showed that the expansion coefficients of the IR basis functions can be calculated with high accuracy from the values of Green's functions for a small number of sampling points. This makes it possible to efficiently transform data between the imaginary time and imaginary frequency spaces. In this section, we show how the sparse sampling method can be used to efficiently solve the diagrammatic equations.

4.1 Noble-gas atoms, silicon crystals: Self-consistent GW and second-order perturbation (GF2) calculations

From Ref. [12], which proposed a sparse sampling method, we present the results of a self-consistent GW calculation and a benchmark calculation using second-order perturbations (GF2). The purpose of this study was to verify the stability and accuracy of the numerical calculations. Thus, they chose the physically “trivial” but technically difficult noble gas atoms and silicon crystals. In this article, we present the results for noble gases. Please refer to the original paper [12] for the results for silicon crystals.

We consider the Hamiltonian

$$H = \sum_{ij\sigma} h_{ij} c_{i\sigma}^\dagger c_{j\sigma} + \frac{1}{2} \sum_{ijkl} \sum_{\sigma\sigma'} V_{ijkl} c_{i\sigma}^\dagger c_{k\sigma'}^\dagger c_{l\sigma'} c_{j\sigma}, \quad (15)$$

where h_{ij} is the non-interacting Hamiltonian; V_{ijkl} is the Coulomb integral; i, j, k , and l are orbital indices; and σ and σ' are spin indices. In this case, the Dyson equation is as follows:

$$\hat{G}(i\omega_n^F) = [(i\omega_n^F + \mu)I - F - \hat{\Sigma}(i\omega_n^F)]^{-1}, \quad (16)$$

where the Fock matrix is given by $F = h + \Sigma^{\text{HF}}$. The Hartree-Fock term can be computed as

$$\Sigma_{ij}^{\text{HF}} = (2V_{ijkl} - V_{ilkj})\rho_{kl}, \quad (17)$$

where we used Einstein's notation. We use different $\hat{\Sigma}(i\omega_n^F)$ for different approximations. Based on the GF2 theory, we use

$$\begin{aligned} \tilde{\Sigma}_{ij}(\tau) &\simeq \Sigma_{ij}^{(2)}(\tau) = -G_{kl}(\tau)G_{qm}(\tau)G_{np}(-\tau) \\ &\times V_{ikpq}(2V_{ljmn} - V_{mjl}). \end{aligned} \quad (18)$$

In the GW approximation, we take

$$\tilde{\Sigma}_{ij}(\tau) \simeq \Sigma_{ij}^{GW}(\tau) = -G_{lk}(\tau)\tilde{W}_{ilkj}(\tau). \quad (19)$$

Here, $\tilde{W} = W - V$ is the dynamic part of the screened interaction W :

$$\hat{W}_{ijkl}(i\omega_n^B) = V_{ijkl} + V_{ijpq}\hat{P}_{qpsr}(i\omega_n^B)\hat{W}_{rskl}(i\omega_n^B). \quad (20)$$

The bare polarization function is given by

$$P_{ijkl}(\tau) = -G_{il}(\tau)G_{jk}(-\tau). \quad (21)$$

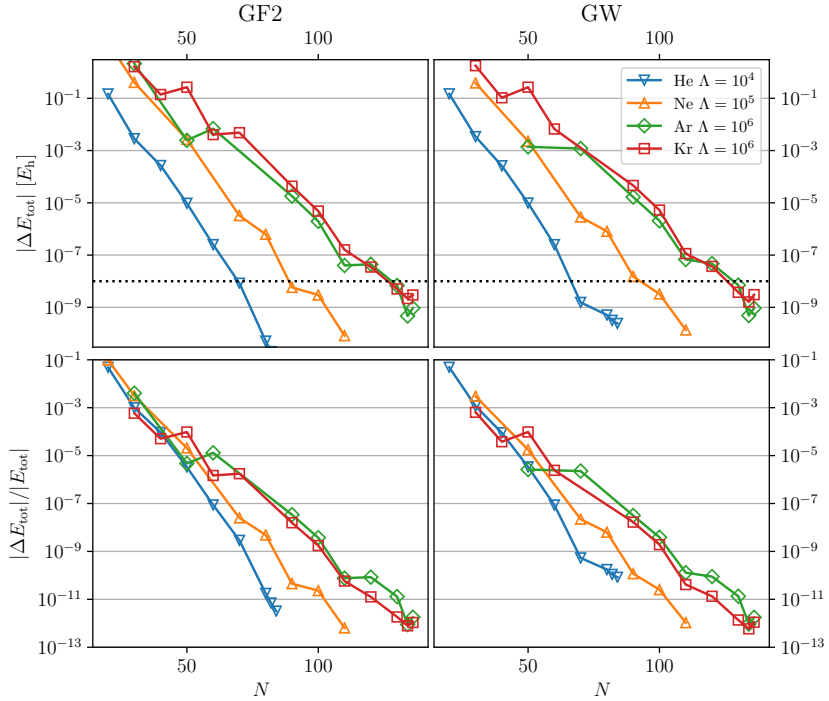


Figure 6: Convergence of total energy in GF2 (left panel) and *GW* (right panel) calculations for noble gas atoms. The horizontal axis is the number of IR bases. The upper panel shows the absolute error of the energy (in Hartree E_h), and the lower panel shows the relative error. From Ref. [12].

Equations (16)–(21) are diagonal in the imaginary frequency or imaginary time. Therefore, if the IR expansion coefficients of the response functions appearing on the right-hand side of each of are known, the values of the left-hand side can be calculated quickly on the sampling points and then immediately converted into the IR basis. Thus, by going through the IR basis, we can conduct self-consistent calculations while keeping the data compact.

Figure 6 shows the results of the calculation using the all-electron basis (cc-pVDZ) for noble-gas atoms ($\beta = 1000 E_h^{-1}$, $T \simeq 316$ K). Owing to the deep core state of noble gas atoms, it is difficult to apply all-electron calculations on a conventional polynomial basis, which requires thousands of basis functions even with the introduction of an effective potential. However, by combining the IR basis with sparse sampling, we can conduct all-electron calculations with as few as 100 basis functions.

As the number of basis functions L increases, the total energy converges exponentially, with relative errors easily converging below the level of 10^{-10} . For heavier noble-gas atoms, the core states deepen. The IR basis can easily handle these deep core states by increasing $\Lambda = \beta\omega_{\max}$. The results of the *GW* method, which involves the treatment of the response functions of both fermions and bosons, also show convergence comparable to that of GF2. This indicates the high numerical stability of the method.

4.2 First-principles calculations of superconducting transition temperature based on Migdal-Eliashberg equation

The transition temperature (T_c) of a conventional (phonon-mediated) superconductor was recently obtained from first-principles calculations. The main theoretical approaches are the superconducting density functional theory and the Migdal-Eliashberg theory, the latter of which has the advantage in that the effective mass renormalization owing to the electron-phonon interaction can be determined self-consistently. By contrast, a realistic prediction of the transition temperature is extremely difficult at low temperatures because it requires simultaneous treatment of a phonon-mediated attraction and Coulomb repulsion, the energy scales of which are two or three orders of magnitude different. In this section, we introduce a recent study [23], which tackles this problem using an IR basis.

In the framework of the Migdal-Eliashberg theory, T_c is obtained by solving the following linearized gap equation:

$$\tilde{\lambda}\Delta_i(i\omega_n) = -T \sum_{j\omega'_n} K_{ij}(i\omega_n - i\omega'_n)F_j(i\omega'_n). \quad (22)$$

Here, subscript i denotes the momentum and band index, Δ_i is the superconducting gap function, and $K_{ij} = K_{ij}^{\text{el-ph}} + K_{ij}^{\text{el-el}}$ denotes the electron-phonon and (screened) Coulomb interaction. Because the anomalous Green's function F_i is given by

$$F_i(i\omega_n) = |G_i(i\omega_n)|^2 \Delta_i(i\omega_n).I \quad (23)$$

Equation (22) is an eigenvalue problem for a matrix, and $\tilde{\lambda}$ is its eigenvalue. The general framework of the theory aims to solve Eq. (22) using G_i , including the self-energy correction by $K_{ij}^{\text{el-ph}}$, and identify T_c as the temperature at which the maximum value of $\tilde{\lambda}$ reaches 1.

Because the convolution integrals of the boson and fermion Green's functions are diagonal in imaginary time, the IR basis and the sparse sampling method can be applied to this problem. In general, because realistic materials contain a large number of bands, and the number of k -points required for convergence is large at low temperatures, it is difficult to calculate Eq. Using the IR basis, we can expect a dramatic improvement, as shown in Table 1.

The actual eigenvalues of the linearized gap equation $\tilde{\lambda}$ for BCC-Nb and cubic LaH_{10} under high pressure (250 GPa) are shown in Fig. 7. The calculated temperatures are 19.7 and 271.6 K, respectively, which are slightly higher than the respective transition temperatures. Figure 7(a) shows the conventional method (imaginary frequency + FFT), which converges roughly at $N_\omega = 512$ for LaH_{10} , but still does not converge at $N_\omega = 2048$ for Nb. As a rough estimate, if we assume that the upper limit of the band is $\omega_{\text{max}} \sim 10$ eV, which leads to $\beta\omega_{\text{max}} \simeq 10^4$, we will need a higher N_ω to converge for Nb. However, with the IR basis + sparse sampling method shown in Figure 7(b), we already have a fully converged value at $\Lambda = 10^4$. Comparing the two calculations with $N_\omega = 4096$ (shown in Ref. [23]) and $\Lambda = 10^5$ as an example, we found that the number of bases is $L = 138$, which saves approximately 30-times the amount of memory and improves the actual calculation speed by approximately 20-fold. We note that we did not successfully obtain converged self-consistent solutions for $\Lambda < 10^2$ (LaH_{10}) and $\Lambda < 10^4$ (Nb), which may be because Λ was not large enough (refer to Appendix B). In the present calculation, the static shielding Coulomb interaction is used as the electron-electron interaction, but it can be extended to include the plasmon effect in the random phase approximation.

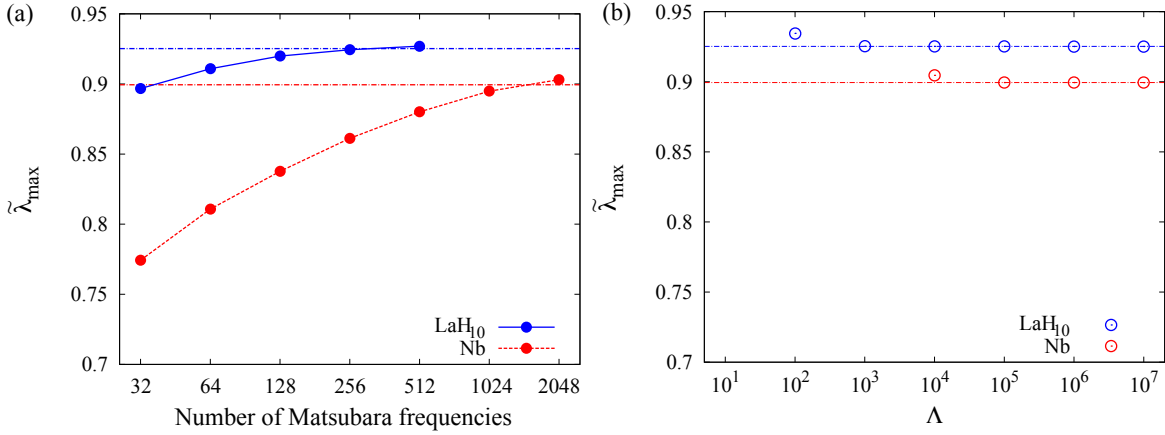


Figure 7: The convergence of the maximum eigenvalue $\tilde{\lambda}_{\max}$ of the linearized gap equation is just above the transition temperature. (a) Imaginary frequency + FFT and (b) IR basis + sparse modeling. The chain line in the figure shows the value obtained using the IR basis. This plot is essentially the same as Fig. 2 of Ref. [23]. The minor differences in the values of $\tilde{\lambda}_{\max}$ originate from differences in implementation details.

4.3 Calculation of magnetic interaction based on Lichtenstein formula

As is well known, density functional theory (DFT) is applicable only to the ground state, and it is impossible to calculate the properties of finite temperatures without modification. In the case of magnetic materials, the magnitude of the magnetic moment at absolute zero can be predicted; however, the transition temperature cannot be calculated. Although there are several approaches to this problem, the most convenient and commonly used approach is to derive an effective spin model from the results of the electronic state calculation, and to obtain the transition temperature by a calculation using the spin model (*e.g.*, mean-field approximation and Monte Carlo calculation). Among the mappings to the spin model [24], a method called the Lichtenstein method, has been found to significantly improve the efficiency of the calculation by using the IR basis + sparse sampling method, which is briefly introduced in this section [13–15].

In this theory, we compute the interaction parameters J_{ij} in the Heisenberg-type spin model $H = -2 \sum_{\langle i,j \rangle} J_{ij} \mathbf{S}_i \cdot \mathbf{S}_j$ as follows:

$$J_{ij} = -\frac{T}{2} \sum_{\omega_n} \text{Tr}[G_{ij}(i\omega_n) M_j G_{ji}(i\omega_n) M_i]. \quad (24)$$

Here, G_{ij} is Green's function for an effective tight-binding model derived from DFT calculations, and i, j are site indices. When the number of orbitals belonging to site i is N_{orb}^i , G_{ij} is an $N_{\text{orb}}^i \times N_{\text{orb}}^j$ matrix. In addition, although M_i is a perturbation term to the Hamiltonian owing to the infinitesimal rotation of the spins, here it should simply be regarded as a constant matrix of $N_{\text{orb}}^i \times N_{\text{orb}}^i$, which does not depend on ω_n . Moreover, Tr in Eq. (24) denotes the trace regarding the orbital component. Considering the computational cost required to evaluate this term, the dominant factor is the Fourier transform of the Green's function from the k space to the real space, which is approximately $O(cN_{\omega})$ using the usual Matsubara frequency mesh. Here, the coefficient factor c is approximately $c = O((N_k \log N_k)^3 N_{\text{orb}}^2)$ when

the number of k meshes in one dimension is N_k . By contrast, if Green's function calculation is limited to the sparse grid, the computational cost becomes approximately $O(cL)$, which is much lower at low temperatures. In the actual calculation, the trace of Eq. (24) is calculated on the sparse grid and finally converted into the IR basis. Subsequently, Eq. (24) is obtained by recovering the values at the imaginary time $\tau = 0$ from the expansion coefficients in the IR basis. In this method, the loss in the basis conversion is almost negligible, and the computation time can be reduced by a factor of N_ω/L .

In this study, although we used the Liechtenstein method as an example, we can generally apply this method for the free energy $F[A]$ of a system described by the second-order Hamiltonian $H = \sum_{12} A_{12} c_1^\dagger c_2$, with the derivative $\delta_{A_{12}} F$, $\delta_{A_{12}} \delta_{A_{34}} F$, \dots with respect to A . Although this computation is not extremely heavy, it is a good example showing that the IR basis can be used as a common tool. As we have seen, the convergence of the calculations using the IR basis is extremely high, and the number of parameters required to check the convergence can be reduced, which is always a significant advantage in research using numerical calculations.

4.4 Other applications

In addition to those introduced in this paper, there are many other applications in the field of *ab initio* calculations, such as the calculation of the superconducting transition temperature using the FLEX approximation [17], *ab initio* calculations of NiO compounds based on the self-energy embedding method [16], and an *ab initio* estimation of the magnetic interaction constant of NdNiO₂ [15]. The exponential convergence of the calculation accuracy with respect to the basis size is also useful in model calculations, such as self-energy denoising [25] and efficient discretization of quantum impurity problems [26].

5 `irbasis` library

In the previous sections, we described the IR basis and sparse sampling method. We developed the library `irbasis` [18], allowing these new techniques to be easily used without knowing the details of the computation of the IR basis functions and sampling points. Here is an overview of `irbasis` and a brief description of its usage. In addition, although `irbasis` is available in both `Python` and `C++`, we focus on the `Python` version, which implements sparse sampling. Once the values of the basis functions and the sampling points are written to a file, diagram calculations using sparse sampling can be conducted in any programming language (the superconductivity calculations described above were actually applied in Fortran).

5.1 Installation

Because `irbasis` is registered to PyPI, its installation is quite simple and can be achieved by running the following command from a shell:

```
$ pip install -U irbasis
```

The `-U` option aims to update to the latest version of `irbasis` if it is already installed.

5.2 Dimensionless form

In practice, the IR basis function can be computed by solving certain integral equations [27]. The accurate computation of the basis functions for small singular values, however, requires multiple-precision arithmetic. Thus, solving an integral equation on the fly is currently impractical. Therefore, `irbasis` contains precomputed high-precision data of IR basis functions for typical parameters $\Lambda \equiv \beta\omega_{\max} = 10, 10^2, \dots, 10^7$, and $s_l^\alpha/s_0^\alpha > 10^{-15}$.

Here, `irbasis` uses the dimensionless convention $u_l^\alpha(x)$, $v_l^\alpha(y)$, and s_l^α [18], which are related with the original convention as

$$U_l^\alpha(\tau) = \sqrt{\frac{2}{\beta}} u_l^\alpha(x(\tau)), \quad (25)$$

$$V_l^\alpha(\omega) = \sqrt{\frac{1}{\omega_{\max}}} v_l^\alpha(y(\omega)), \quad (26)$$

$$S_l^\alpha = \sqrt{\frac{\beta\omega_{\max}^{1+2\delta_{\alpha,B}}}{2}} s_l^\alpha, \quad (27)$$

$$\hat{U}_l^\alpha(i\omega_n) = \sqrt{\beta} u_{nl}^\alpha. \quad (28)$$

Here, $x(\tau) = 2\tau/\beta - 1 \in [-1, 1]$ and $y(\omega) = \omega/\omega_{\max} \in [-1, 1]$, and we define

$$u_{nl}^\alpha \equiv \frac{1}{\sqrt{2}} \int_{-1}^1 dx e^{i\pi\{n+(1/2)\delta_{\alpha,F}\}(x+1)} u_l^\alpha(x). \quad (29)$$

We fix the sign of the IR basis functions by $u_l^\alpha(1) > 0$. Note that $u_l^\alpha(x) = (-1)^l u_l^\alpha(x)$, $v_l^\alpha(y) = (-1)^l v_l^\alpha(-y)$. The computation of u_{nl}^α is implemented in the library.

5.3 Evaluation of IR basis functions

Below is an example code [28] that loads the basis data of $\Lambda = 1000$ (fermion) and computes the basis functions at certain values of x , y , and imaginary frequency n . The function `load` loads the basis function data into memory and creates a basis object. By calling the member functions of this basis object, various values can be evaluated. For example, `s1` returns s_l^α as a one-dimensional array. In addition, `ulx` and `vly` evaluate $u_l^\alpha(x)$ and $v_l^\alpha(y)$, respectively, `d_ulx` and `d_vly` evaluate their (higher-order) derivatives $\frac{\partial^k u_l^\alpha(x)}{\partial x^k}$ and $\frac{\partial^k v_l^\alpha(y)}{\partial y^k}$, and `compute_unl` evaluates u_{nl}^α .

```
import irbasis
import numpy

b = irbasis.load('F', 1000)
print("dim: ", b.dim())

# All singular values
print("singular values: ", b.s1())
print("u_0(0.1)", b.ulx(0, 0.1))
print("v_0(0.1)", b.vly(0, 0.1))

print("k-th derivative of u_l(x) and v_l(y)")
for k in range(1,3):
    print(" ", k, b.d_ulx(0, 0.1, k))
    print(" ", k, b.d_vly(0, 0.1, k))
```

```
Compute u_{nl} as a matrix for the first
# 10 non-native Matsubara frequencies
unl = b.compute_unl(numpy.arange(10))
print("matrix unl ", unl.shape)
```

When running this, you will instantly obtain the following results.

```
dim: 72
singular values: [6.93676632e-02 6.39029304e-02 4.73525981e-02 3.78765556e-02
 2.69709397e-02 1.97919952e-02 1.38987851e-02 9.79170114e-03
 6.77586537e-03 4.66563008e-03 3.18095991e-03 2.15479043e-03
 1.44908097e-03 9.68433898e-04 6.43222579e-04 4.24765651e-04
 2.78944576e-04 1.82210441e-04 1.18411677e-04 7.65700139e-05
 4.92756267e-05 3.15628325e-05 2.01254341e-05 1.27758728e-05
 8.07529293e-06 5.08266091e-06 3.18587477e-06 1.98887606e-06
 1.23669448e-06 7.65992957e-07 4.72633737e-07 2.90529576e-07
 1.77929561e-07 1.08573268e-07 6.60143404e-08 3.99959952e-08
 2.41478607e-08 1.45293028e-08 8.71232105e-09 5.20671801e-09
 3.10136291e-09 1.84126342e-09 1.08960675e-09 6.42730925e-10
 3.77927545e-10 2.21524423e-10 1.29443906e-10 7.54051848e-11
 4.37917794e-11 2.53552246e-11 1.46364946e-11 8.42388202e-12
 4.83396492e-12 2.76580014e-12 1.57787966e-12 8.97577822e-13
 5.09125136e-13 2.87965124e-13 1.62415181e-13 9.13467044e-14
 5.12326226e-14 2.86546680e-14 1.59825721e-14 8.89012035e-15
 4.93157043e-15 2.72826291e-15 1.50527941e-15 8.28293591e-16
 4.54562830e-16 2.48800912e-16 1.35820168e-16 7.39497064e-17]
u_0(0.1) 0.27401896348952326
v_0(0.1) 0.7859154340971242
k-th derivative of u_1(x) and v_1(y)
 1 0.04705147674680368
 1 -5.044715458614918
 2 0.4853426135802095
 2 76.97205690788114
unl (10, 72)
```

One can evaluate the basis functions for multiple values of x , y , or n with a single function call (corresponding to numpy broadcasting, see the examples below).

5.4 Example: Second-order perturbation theory

As a simple example, we calculate the self-energy of the two-dimensional Hubbard model within the range of second-order perturbations. The following code is available as a Jupyter notebook [29].

First, for $\beta = 10^3$ and $\omega_{\max} = 10^2$ ($\Lambda = 10^5$), we calculate the data required for the calculation, the positions of the sampling points, and the values of the basis functions: \mathbf{F}_α^+ in Eqs. (13) and (14), and $\hat{\mathbf{F}}_\alpha^+$ in Eqs. (13) and (14). Note that the sampling-point-generating functions (`sampling_points_x`, `sampling_points_matsubara`) take the index of the highest order of the basis function used for the expansion (number of basis functions -1) as an argument. In this sample, we used all 137 basis functions stored in the library.

After executing the code below, the variables `invFtau` and `invhatF` point to two-dimensional arrays of \mathbf{F}_α^+ and $\hat{\mathbf{F}}_\alpha^+$, respectively.

```
import irbasis
import numpy as np
```

```

beta = 20.0
Lambda = 10000.0
wmax = Lambda/beta
print("wmax", wmax)

b = irbasis.load('F', wmax * beta)
dim = b.dim()

# Sampling points in x
sp_x = b.sampling_points_x(whichl=dim-1)
print(sp_x)

Sampling frequencies in n
sp_n = b.sampling_points_matsubara(whichl=dim-1)
print(sp_n)

all_ls = np.arange(dim)

# Compute F and the pseudo-inverse
# for imaginary time
Ftau = np.sqrt(2/beta) * \
    b.ulx(all_ls[:, None], sp_x[None, :]).T
invFtau = np.linalg.pinv(Ftau)

# Compute F and the pseudo-inverse
# for imaginary frequency
hatF = np.sqrt(beta) * b.compute_unl(sp_n)
invhatF = np.linalg.pinv(hatF)

```

We now compute the Green's function for a band dispersion:

$$\epsilon(k) = -2(\cos k_1 + \cos k_2). \quad (30)$$

Note that the Green' function

$$G(k, i\omega) = \frac{1}{i\omega - \epsilon(k)} \quad (31)$$

is computed only on the sampling frequencies.

```

# Parameters
nk_lin = 64
U, kps = 2.0, np.array([nk_lin, nk_lin])
nw = len(sp_n)
ntau = len(sp_x)

# Generate k mesh and non-interacting band energies.
nk = np.prod(kps)
kgrid = [2*np.pi*np.arange(kp)/kp for kp in kps]
k1, k2 = np.meshgrid(*kgrid, indexing='ij')
ek = -2*(np.cos(k1) + np.cos(k2))
iw = 1j*np.pi*(2*sp_n+1)/beta

# G(iw, k): (nw, nk)
gkf = 1.0 / (iw[:,None] - ek.ravel()[:,None])

```

At this point, `gkf` is a two-dimensional array of the number of sampling frequencies \times the number of k points. In imaginary time and real spaces, the second-order self-energy is given by

$$\Sigma(\tau, r) = U^2 G^2(\tau, r) G(\beta - \tau, r), \quad (32)$$

where r represents a position in real space. Thus, one can evaluate the self-energy by transforming Green's function from the sampling frequencies to the IR basis and then to the sampling τ points as follows:

```
# G(1, k): (L, nk)
gkl = np.dot(invhatF, gkf)

# G(tau, k): (ntau, nk)
gkt = np.dot(Ftau, gkl)

# G(tau, r): (ntau, nk)
grt = fftn(gkt.reshape(ntau, *kps), axes=(1,2)).\
      reshape(ntau, nk)

# Sigma(tau, r): (ntau, nk)
srt = U*U*grt*grt*grt[:, :-1, :]
```

At this point, the computed self-energy $\Sigma(\tau, r)$ is stored in a two-dimensional array `srt`. Finally, we transform the self-energy into sampling frequencies (through the IR basis) and momentum space as follows:

```
# Sigma(1, r): (L, nk)
srl = np.dot(invFtau, srt)

# Sigma(iw, r): (nw, nk)
srf = np.dot(hatF, srl)

# Sigma(iw, k): (nw, kps[0], kps[1])
srf = srf.reshape(len(sp_n), *kps)
skf = ifftn(srf, axes=(1,2))/nk**2
```

Figure 8 plots the computed self-energy. Self-consistent calculations can be performed on sampling frequencies/imaginary times without using a dense grid.

6 Summary and future perspectives

In this study, we introduced a compact representation of Green's function and a sparse sampling scheme for solving diagrammatic equations. Using the IR basis, the data size increases only logarithmically with respect to the inverse temperature. Furthermore, by using the sparse sampling method, the numerical data remain compact. The sparse sampling method enables us to rapidly solve the diagrammatic equations while keeping the numerical data compact and numerically accurate. These methods are extremely useful in *ab initio* calculations, where we need to deal with wide bandwidths and different energy scales, such as low temperatures. As examples, we present the results of *ab initio* calculations using the *GW* approximation and the Migdal-Eliashberg theory. Furthermore, we have given an overview of the numerical library `irbasis`. We hope that this article will serve as a starting point for applications in

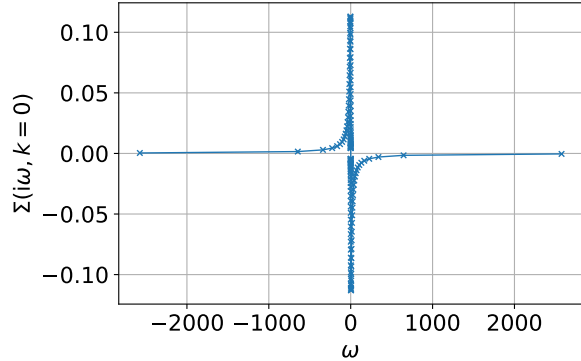


Figure 8: Self-energy computed for the Hubbard model on the sampling frequencies ($k = 0$). In sparse sampling methods, the self-energy is evaluated at a few sampling frequencies.

various fields. If the reader is troubled by problems with the data size and computation time, please consult with us.

Finally, we discuss future perspectives. The frontier of method development has already shifted towards two-particle quantities. There are various theories at the two-particle level: diagrammatic calculations with vertex corrections, dynamical susceptibility calculations based on dynamical mean field theory, and nonlocal extensions of dynamical mean field theory that can handle unconventional superconductivity (such as the dual fermion method [30] and the dynamical vertex approximation approach [31]). These two-particle quantities not only have three augments for imaginary frequencies but also arguments for orbitals, spins, and wavenumbers. To conduct calculations using these theories, we need an efficient numerical treatment of two-particle quantities, which remains a challenging issue. A breakthrough based on the IR basis and the sparse sampling method has recently been made regarding such problems. interested readers are referred to recent articles [19, 32, 33].

We hope that the development of such fundamental numerical techniques will lead to technological breakthroughs and a better understanding of the properties of strongly correlated compounds based on accurate *ab initio* calculations.

Acknowledgments

We would like to thank our collaborators in the research described in this article. Our collaboration with Prof. Masayuki Ozeki, which aims to apply sparse modeling to quantum many-body calculations, led to the discovery of the IR basis.

Funding information This work was supported by the following Grant-in-Aid for Scientific Research: No. 15H05885 (J-Physics), No. 16H01064 (J-Physics), No. 18H04301 (J-Physics), No. 18H01158, No. 16K17735, No. 19K14654, No. 19K14654, No. 21H01003, No. 21H01041. MW acknowledges support by the FWF (Austrian Science Funds) through Project No. P30997. EG and JL were supported by the Simons foundation via the Simons Collaboration on the Many-Electron Problem.

A Some properties of the IR basis functions

In this appendix, we are justifying some of the properties of the IR basis functions discussed in Sec. 2. Let us do this for the fermionic kernel. For this, we will again write the kernel in terms of dimensionless variables, cf. Sec. 5.2:

$$K(x, y) = -\frac{\exp\left(-\frac{\Lambda}{2}xy\right)}{\exp\left(\frac{\Lambda}{2}y\right) + \exp\left(-\frac{\Lambda}{2}y\right)}, \quad (33)$$

where again $x = 2\tau/\beta - 1$, $y = \omega/\omega_{\max}$, and $\Lambda = \beta\omega_{\max}$.

This kernel is clearly square integrable, i.e., $\int_{-1}^1 dx \int_{-1}^1 dy K^2(x, y) < \infty$, since its value is bounded. One can show that any such kernel admits a singular value expansion [34]:

$$K(x, y) = \sum_{l=0}^{\infty} u_l(x) s_l v_l^*(y), \quad (34)$$

where again s_l are the singular values and u_l and v_l are the left and right singular functions, respectively.

First, since the kernel is smooth for any temperature, $K \in C^\infty[-1, 1]^2$, one has that the singular values decay faster than any power asymptotically [34]. Numerically, one can show that s_l in fact decay faster than exponentially, thus establishing Property 1.

The left and right singular functions in turn are the solution to eigenvalue equations with the following integral kernels:

$$K^u(x, x') = \int_{-1}^1 dy K(x, y) K(x', y) = \sum_{n=0}^{\infty} \frac{\Lambda^{2n}}{4n+2} \sum_{k=0}^{2n} \frac{E_k(\frac{1}{2}(x+1)) E_{2n-k}(\frac{1}{2}(x'+1))}{k!(2n-k)!}, \quad (35)$$

$$K^v(y, y') = \int_{-1}^1 dx K(x, y) K(x, y') = \frac{\tanh(\frac{\Lambda}{2}y) + \tanh(\frac{\Lambda}{2}y')}{\Lambda(y+y')}, \quad (36)$$

where $E_n(x)$ is the n -th Euler polynomial.

These kernels are real and symmetric by construction, which implies that the singular functions can be chosen to be real. They are also *centrosymmetric*, i.e., one has $K^u(x, x') = K^u(-x, -x')$. Since s_l are not degenerate (see later), this implies that each $u_l(x)$ must be either an odd or an even function in x . The same is true for $v_l(y)$. This establishes property 3.

The kernel $-K(x, -y)$ belongs to the “exponential family” of parametrized probability distributions. These kernels satisfy a property called strict total positivity [35]. We briefly state this property here: The set of k -samples \mathcal{S}_k into the space $[-1, 1]$ is defined as $\mathcal{S}_k := \{(x_1, \dots, x_k) : -1 \leq x_1 < \dots < x_k \leq 1\}$. A kernel $K : [-1, 1]^2 \rightarrow \mathbb{R}$ is called strictly totally positive (STP) if for any $k \geq 0$ and $(x_1, \dots, x_k), (y_1, \dots, y_k) \in \mathcal{S}_k$, one has

$$\det \begin{pmatrix} K(x_1, y_1) & K(x_1, y_2) & \dots & K(x_1, y_k) \\ \vdots & \vdots & \ddots & \vdots \\ K(x_k, y_1) & K(x_k, y_2) & \dots & K(x_k, y_k) \end{pmatrix} > 0. \quad (37)$$

(This generalizes the notion of positive matrices appearing in, e.g., the theory of finite Markov chains, to integral kernels.) One can now show that since K is a STP kernel, then the following holds [35]:

1. there exists a countable set of singular values which are all non-degenerate,
2. the n -th left/right singular function has exactly n nodal zeros in $(-1, 1)$ and no zeros of another type,
3. the zeros of the n 'th and $n + 1$ 'st singular function strictly interlace, i.e., exactly one zero of u_n falls between two consecutive zeros of u_{n+1} .

This establishes property 4.

B Numerical stability of sparse sampling

When the expansion coefficients are numerically evaluated using the sparse sampling “fitting” procedures, i.e. Eqs. (13) and (14), numerical errors, such as round-off errors from floating point operations or truncation errors from a finite basis cutoff, may be amplified due to the (pseudo-)inversion process. This error amplification can be quantified by the condition number of the transformation matrices \mathbf{F}_α and $\hat{\mathbf{F}}_\alpha$, defined as the product of the 2-norms of the matrix and its inverse. In Fig. 9 we show the behaviors of such condition numbers for the IR basis as a function of the basis size $N = L$ (left panel, compared to the Chebyshev representation), and as a function of Λ (right panel). We can see that up to a significant number of basis functions, the condition numbers are $< 10^4$, which indicates well-conditioned inversion problems. In addition, the condition numbers show an approximate scaling of $O(L^{1/2})$, which is slower than that of the Chebyshev representation $O(L^{3/2})$. Since the values of L and Λ shown in Fig. 9 cover most values used in the calculations reviewed in this paper, the sparse sampling scheme guarantees stable numerical routines to get accurate results.

In practical applications of the sparse sampling method, one should take care not to introduce large systematic errors in the basis representation as defined in Eq. (6), such as large truncation errors ϵ_L due to insufficient basis size L or control parameter Λ . For example, a systematic error at the level of 10^{-3} in the basis representation, amplified by a condition number of 10^3 of the “fitting” procedure, may lead to a numerical error greater than the actual result. As shown in Fig. 10, such a situation could make the simulation unstable. Therefore, to ensure stable numerical calculations with the sparse sampling method, one should choose the appropriate basis parameters L and Λ such that the basis representation stays accurate.

Figure 10 shows examples of stable and unstable GW calculation of the Krypton atom in cc-pVDZ basis with $\beta = 10\,000 E_h^{-1}$ using sparse sampling. We carried out five GW iterations with different choices of Λ , and plotted the norms of G_l from each iteration. The left panel of Fig. 10 shows results for $\Lambda = 10^7$. At each iteration, the Green’s function is well approximated by the IR basis and the basis truncation error is small, resulting in a stable simulation. In the right panel, a smaller $\Lambda = 10^6$ is used, which is insufficient for this system and introduces a large systematic error (around 10^{-3}), while the condition number of \mathbf{F} is $\sim 10^3$. The systematic error is amplified by fitting procedure, rendering the GW simulation unstable.

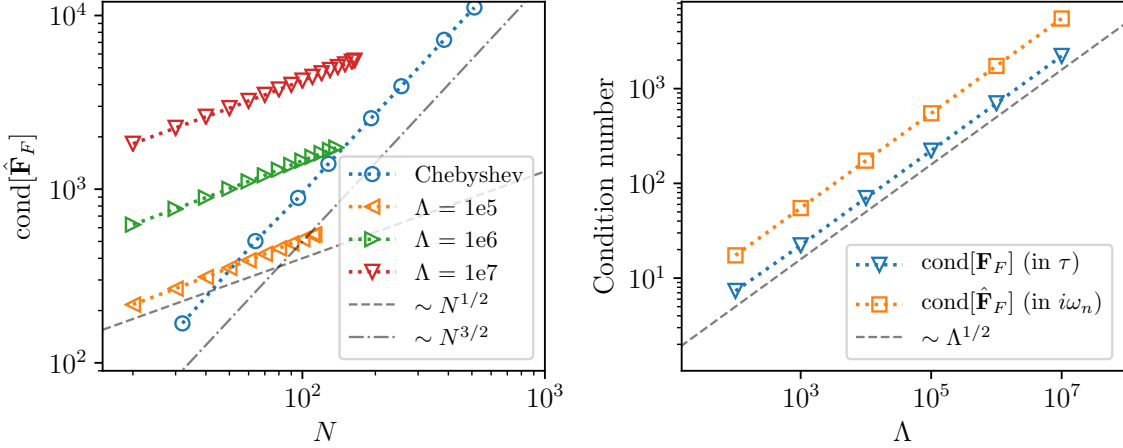


Figure 9: Condition number of the IR transformation matrices $\hat{\mathbf{F}}_F$ and \mathbf{F}_F [12]. Left panel shows the condition number of frequency transformation matrices $\hat{\mathbf{F}}_F$ as a function of basis size $N = L$, in comparison with the Chebyshev representation. Right panel shows the condition number of both τ and $i\omega_n$ transformation matrices with respect to Λ , where N is chosen to be the maximum number of coefficients with the same cutoff in singular values S_l^α , provided in the `irbasis` library [27].

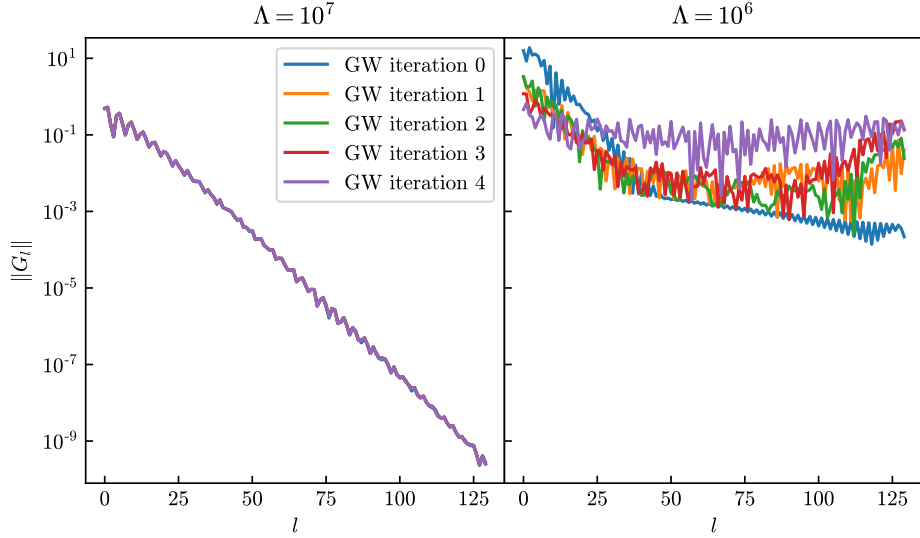


Figure 10: Examples of stable and unstable *GW* calculations of the Krypton atom

References

- [1] H. N. Rojas, R. W. Godby and R. J. Needs, *Space-time method for ab initio calculations of self-energies and dielectric response functions of solids*, Physical Review Letters **74**(10), 1827 (1995), doi:10.1103/physrevlett.74.1827.
- [2] M. Kaltak, J. Klimeš and G. Kresse, *Low Scaling Algorithms for the Random Phase Approximation: Imaginary Time and Laplace Transformations*, Journal of Chemical Theory and Computation **10**(6), 2498 (2014), doi:10.1021/ct5001268.
- [3] N. E. Bickers and D. J. Scalapino, *Conserving approximations for strongly fluctuating electron systems. I. Formalism and calculational approach*, Annals of Physics **193**(1), 206 (1989), doi:10.1016/0003-4916(89)90359-x.
- [4] N. E. Bickers and S. R. White, *Conserving approximations for strongly fluctuating electron systems. II. Numerical results and parquet extension*, Physical Review B **43**(10), 8044 (1991), doi:10.1103/physrevb.43.8044.
- [5] A. Georges, G. Kotliar, W. Krauth and M. J. Rozenberg, *Dynamical mean-field theory of strongly correlated fermion systems and the limit of infinite dimensions*, Reviews of Modern Physics **68**(1), 13 (1996-01), doi:10.1103/revmodphys.68.13.
- [6] E. Gallicchio and B. J. Berne, *The absorption spectrum of the solvated electron in fluid helium by maximum entropy inversion of imaginary time correlation functions from path integral Monte Carlo simulations*, The Journal of Chemical Physics **101**(11), 9909 (1994), doi:10.1063/1.467892.
- [7] A. A. Kananenka, J. J. Phillips and D. Zgid, *Efficient Temperature-Dependent Green's Functions Methods for Realistic Systems: Compact Grids for Orthogonal Polynomial Transforms*, Journal of Chemical Theory and Computation **12**(2), 564 (2016), doi:10.1021/acs.jctc.5b00884.
- [8] M. Schüller and Y. Pavlyukh, *Spectral properties from Matsubara Green's function approach: Application to molecules*, Physical Review B **97**(11), 115164 (2018), doi:10.1103/physrevb.97.115164, 1710.08660.
- [9] T. Y. Takeshita, W. Dou, D. G. A. Smith, W. A. d. Jong, R. Baer, D. Neuhauser and E. Rabani, *Stochastic resolution of identity second-order Matsubara Green's function theory*, The Journal of Chemical Physics **151**(4), 044114 (2019), doi:10.1063/1.5108840.
- [10] H. Shinaoka, J. Otsuki, M. Ohzeki and K. Yoshimi, *Compressing Green's function using intermediate representation between imaginary-time and real-frequency domains*, Physical Review B **96**(3), 035147 (2017), doi:10.1103/physrevb.96.035147.
- [11] J. Otsuki, M. Ohzeki, H. Shinaoka and K. Yoshimi, *Sparse modeling approach to analytical continuation of imaginary-time quantum Monte Carlo data*, Physical Review E **95**(6), 061302(R) (2017), doi:10.1103/physreve.95.061302.
- [12] J. Li, M. Wallerberger, N. Chikano, C.-N. Yeh, E. Gull and H. Shinaoka, *Sparse sampling approach to efficient ab initio calculations at finite temperature*, Physical Review B **101**(3), 035144 (2020), doi:10.1103/physrevb.101.035144.

- [13] T. Nomoto, T. Koretsune and R. Arita, *Local force method for the ab initio tight-binding model: Effect of spin-dependent hopping on exchange interactions*, Physical Review B **102**(1), 014444 (2020), doi:10.1103/physrevb.102.014444, 2003.11162.
- [14] T. Nomoto, T. Koretsune and R. Arita, *Formation Mechanism of the Helical Q Structure in Gd-Based Skyrmiion Materials*, Physical Review Letters **125**(11), 117204 (2020), doi:10.1103/physrevlett.125.117204, 2003.13167.
- [15] Y. Nomura, T. Nomoto, M. Hirayama and R. Arita, *Magnetic exchange coupling in cuprate-analog d9 nickelates*, Physical Review Research **2**(4), 043144 (2020), doi:10.1103/physrevresearch.2.043144, 2006.16943.
- [16] S. Iskakov, C.-N. Yeh, E. Gull and D. Zgid, *Ab initio self-energy embedding for the photoemission spectra of NiO and MnO*, Physical Review B **102**(8), 085105 (2020), doi:10.1103/physrevb.102.085105, 2003.04440.
- [17] N. Witt, E. G. C. P. van Loon, T. Nomoto, R. Arita, and T. Wehling, arXiv:2012.04562.
- [18] N. Chikano, K. Yoshimi, J. Otsuki and H. Shinaoka, *irbasis: Open-source database and software for intermediate-representation basis functions of imaginary-time Green's function*, Computer Physics Communications **240**, 181 (2018), doi:10.1016/j.cpc.2019.02.006, 1807.05237.
- [19] H. Shinaoka, J. Otsuki, K. Haule, M. Wallerberger, E. Gull, K. Yoshimi and M. Ohzeki, *Overcomplete compact representation of two-particle Green's functions*, Physical Review B **97**(20), 205111 (2018), doi:10.1103/physrevb.97.205111.
- [20] L. Boehnke, H. Hafermann, M. Ferrero, F. Lechermann and O. Parcollet, *Orthogonal polynomial representation of imaginary-time Green's functions*, Physical Review B **84**(7), 075145 (2011-08), doi:10.1103/physrevb.84.075145.
- [21] J. Otsuki, M. Ohzeki, H. Shinaoka and K. Yoshimi, *Sparse Modeling in Quantum Many-Body Problems*, Journal of the Physical Society of Japan **89**(1), 012001 (2020), doi:10.7566/jpsj.89.012001.
- [22] M. Kaltak and G. Kresse, *Minimax isometry method: A compressive sensing approach for Matsubara summation in many-body perturbation theory*, Physical Review B **101**(20), 205145 (2020), doi:10.1103/physrevb.101.205145, 1909.01740.
- [23] T. Wang, T. Nomoto, Y. Nomura, H. Shinaoka, J. Otsuki, T. Koretsune and R. Arita, *Efficient ab initio Migdal-Eliashberg calculation considering the retardation effect in phonon-mediated superconductors*, Physical Review B **102**(13), 134503 (2020), doi:10.1103/physrevb.102.134503.
- [24] A. I. Liechtenstein, M. I. Katsnelson and V. A. Gubanov, *Exchange interactions and spin-wave stiffness in ferromagnetic metals*, Journal of Physics F: Metal Physics **14**(7), L125 (1984), doi:10.1088/0305-4608/14/7/007.
- [25] Y. Nagai and H. Shinaoka, *Smooth Self-energy in the Exact-diagonalization-based Dynamical Mean-field Theory: Intermediate-representation Filtering Approach*, Journal of the Physical Society of Japan **88**(6), 064004 (2019), doi:10.7566/jpsj.88.064004.

- [26] H. Shinaoka and Y. Nagai, *Sparse modeling of large-scale quantum impurity models with low symmetries*, Physical Review B **103**(4), 045120 (2021), doi:10.1103/physrevb.103.045120.
- [27] N. Chikano, J. Otsuki and H. Shinaoka, *Performance analysis of a physically constructed orthogonal representation of imaginary-time Green's function*, Physical Review B **98**(3), 035104 (2018), doi:10.1103/physrevb.98.035104.
- [28] [https://nbviewer.jupyter.org/github/SpM-lab/ir_kotaibutsuri/blob/82d34fe0bd7f5313fbdfa87a38983aadba2d85cb/sample.ipynb/](https://nbviewer.jupyter.org/github/SpM-lab/ir_kotaibutsuri/blob/82d34fe0bd7f5313fbdfa87a38983aadba2d85cb/sample.ipynb).
- [29] https://nbviewer.jupyter.org/github/SpM-lab/ir_kotaibutsuri/blob/82d34fe0bd7f5313fbdfa87a38983aadba2d85cb/second_order_perturbation.ipynb/.
- [30] A. N. Rubtsov, M. I. Katsnelson and A. I. Lichtenstein, *Dual fermion approach to nonlocal correlations in the Hubbard model*, Physical Review B **77**(3), 033101 (2008), doi:10.1103/physrevb.77.033101.
- [31] A. Toschi, A. Katanin and K. Held, *Dynamical vertex approximation: A step beyond dynamical mean-field theory*, Physical Review B **75**(4), 045118 (2007-01), doi:10.1103/physrevb.75.045118.
- [32] H. Shinaoka, D. Geffroy, M. Wallerberger, J. Otsuki, K. Yoshimi, E. Gull and J. Kuneš, *Sparse sampling and tensor network representation of two-particle Green's functions*, SciPost Physics **8**(1), 012 (2020), doi:10.21468/scipostphys.8.1.012.
- [33] M. Wallerberger, H. Shinaoka and A. Kauch, arXiv:2012.05557v1.
- [34] P. C. Hansen, *Discrete Inverse Problems: Insights and Algorithms*, SIAM, ISBN 978-0-898716-96-2, doi:10.1137/1.9780898718836 (2010).
- [35] S. Karlin, *Total Positivity*, Stanford University Press, ISBN 978-0804703147 (1968).